Title
A Distributed Lumped Parameter Model of Blood Flow

Permalink
https://escholarship.org/uc/item/41q3q2nk

Authors
Mirramezani, Mehran
Shadden, Shawn C

A distributed lumped parameter model of blood flow

Mehran Mirramezani[1,2], **Shawn C. Shadden**[1]

[1]Mechanical Engineering, University of California, Berkeley, CA, USA 94720

[2]Mathematics, University of California, Berkeley, CA, USA 94720

Abstract

We propose a distributed lumped parameter (DLP) modeling framework to efficiently compute blood flow and pressure in vascular domains. This is achieved by developing analytical expressions describing expected energy losses along vascular segments, including from viscous dissipation, unsteadiness, flow separation, vessel curvature and vessel bifurcations. We apply this methodology to solve for unsteady blood flow and pressure in a variety of complex 3D image-based vascular geometries, which are typically approached using computational fluid dynamics (CFD) simulations. The proposed DLP framework demonstrated consistent agreement with CFD simulations in terms of flow rate and pressure distribution, with mean errors less than 7% over a broad range of hemodynamic conditions and vascular geometries. The computational cost of the DLP framework is orders of magnitude lower than the computational cost of CFD, which opens new possibilities for hemodynamics modeling in timely decision support scenarios, and a multitude of applications of imaged-based modeling that require ensembles of numerical simulations.

Keywords

reduced order modeling; image-based computational fluid dynamics; hemodynamics

1 Introduction

Image-based computational fluid dynamics (CFD) is the modeling standard to study patient-specific blood flow features in the cardiovascular system [46]. Applications of image-based CFD are numerous, and include assessment of pathologies, such as vascular stenosis [45, 26], aneurysms [2, 27] and dissection [49, 51], as well as for surgical planning [29, 38] and the evaluation of medical devices [43, 8]. This technology has grown considerably over the last decade, gaining recent FDA approval and clinical adoption [45]. Although image-based

CFD enables comprehensive analysis of hemodynamics, it is computationally expensive, prone to numerical instabilities, and can be sensitive to method parameters. These factors have limited broader translation of image-based CFD to clinical settings, and have limited the ability to perform parametric analyses in cardiovascular applications such as uncertainty quantification, sensitivity analysis, data assimilation, optimization, parameter tuning, etc. Such ensemble-based studies are becoming crucial as hemodynamics modeling matures from proof-of-concept to a paradigm in healthcare technology [31]. These factors motivate the need for reduced-order models (ROMs) of blood flow to be used in place of, or in conjunction with, fully-resolved CFD modeling.

ROMs can roughly be divided into fitting methods (polynomial chaos, machine learning, etc.) or simplified physics models. The work herein focuses on the latter. The most basic simplified physics ROMs are lumped parameter network (LPN) models [47]. Like the Navier-Stokes equations, LPNs describe a mathematical relationship between flow, pressure and their derivatives. Mathematically, LPNs are described by ordinary differential equations (ODEs) or algebraic equations (AEs). Physically, LPNs are often interpreted as electrical circuit analogs where flow and pressure are analogous to current and voltage. The simplest example is a vascular network modeled as a resistor, whereby flow is proportional to pressure drop. Adding a capacitor (RC model) or second resistor (RCR model) are popular extensions, and more elaborate LPNs have been proposed [47, 30, 23]. LPNs are generally used to model complete vascular territories, and by construction, continuous spatial variations in flow and pressure are not resolved. To resolve continuous spatial variations in flow and pressure, the most common ROM approach is to cross-sectionally average the Navier-Stokes equations [6, 22] to generate quasi-ID equations. This approach has been used extensively over the past decades to model hemodynamics [42, 9]. Similarly, more comprehensive 2D models, e.g., [19], have also been proposed. Both quasi-1D or 2D models are described by PDEs, and are thus more computationally expensive than LPN models, and more prone to numerical artifacts and instability [1]. Perhaps more importantly, physics-based ROMs have struggled to accurately predict complex hemodynamic conditions typically observed in image-based vascular models, which is why CFD (using the 3D Navier-Stokes equations) has prevailed in this area.

Our goal is to develop a physics-based model to described distributed changes in hemodynamics, particularly in image-based vascular models, at substantially reduced computational cost and complexity compared to PDE-based approaches to modeling blood flow. Toward this goal, we present a generalized distributed lumped parameter (DLP) framework to compute flow and pressure dynamics in blood vessels by taking into account various sources of energy dissipation. This approach results in ODEs that are significantly easier to solve than existing PDE models, yet it can convey distributed changes in hemodynamics. Moreover, it provides reasonable predictions even in scenarios of complex, 3-dimensional flow where most existing physics-based ROMs provide poor predictions. To evaluate the utility of the proposed DLP methodology, we have applied this framework to a diverse range of healthy and diseased patient-specific cardiovascular anatomies including aortic, aorto-femoral, cerebrovascular, coronary, pulmonary and congenital heart disease surgery models, and have compared DLP predictions of flow and pressure to the "gold-standard" values from 3D time-dependent CFD simulations. To the best of our knowledge,

this is the most comprehensive comparison of a ROM to the current standard of image-based hemodynamics modeling.

2 Methods

Similar to most fluid mechanic models, we aim to develop a relationship between flow and pressure from conservation of mass and balance of momentum principles. Our formulation is in terms of cross-sectionally averaged pressure $P(x, t)$ and volumetric flow rate $Q(x, t)$, where x denotes the axial coordinate along a given vessel and t is time. We assume to be modeling flow within a vascular network, and as such, conservation of mass is imposed at vessel junctions as

$$\sum Q_{in} = \sum Q_{out} \tag{1}$$

The following balance of momentum is assumed to hold along any vascular segment

$$\left(\frac{\rho}{\pi} \int_0^L \frac{1}{R(x)^2} dx \right) \frac{\partial Q}{\partial t} + \mathscr{R}Q + \Delta P = 0 \tag{2}$$

where ρ is fluid density, $R(x)$ is vessel radius assumed to vary axially, L is the length of the vascular segment, and $\mathscr{R}$ represents a generalized resistance. Below we develop an expression for $\mathscr{R}$ by considering expected sources of energy dissipation.

2.1 Viscous dissipation

Assuming Poiseuille flow, the pressure drop across a cylindrical vessel of length L is given by $\Delta P = \mathscr{R}_v Q$, where $\mathscr{R}_v = 8\mu L / \pi R^4$ is the hydraulic resistance, with μ being the blood viscosity and R being the radius. We first consider an integral form of this equation to better account for variations of radius the vessel length as

$$\mathscr{R}_v = \frac{8\mu}{\pi} \int_0^L \frac{1}{R(x)^4} dx \tag{3}$$

For vessels of non-circular cross-section, $R(x) = \sqrt{A(x) / \pi}$ denotes the effective radius (henceforth radius) at local axial coordinate $x \in (0, L)$.

We note that the Poiseuille law, $P = 8\mu L Q/\pi R^4$, can be viewed a special case of the Darcy-Weisbach equation

$$\Delta P = \lambda_s \frac{\rho}{2} \frac{V^2}{2R} \tag{4}$$

where $V = Q/\pi R^2$ is the average fluid velocity, and λ_s is the viscous friction factor. The viscous friction factor of a straight vessel is $\lambda_s = 64/Re$, which yields Poiseuille's law, where Re denotes Reynolds number. This viewpoint will be used next to incorporate pressure loss due to vessel curvature.

2.2 Curvature

The presence of centrifugal forces in a curved vessel results in a skewed velocity profile, which generally increases viscous dissipation as compared to flow through a straight vessel. Assuming steady and fully developed flow, the viscous friction factor of a curved vessel (λ_c) can be related to the viscous friction factor of a straight vessel (λ_s) with similar length and radius [24]

$$\gamma \doteq \frac{\lambda_c}{\lambda_s} = 0.1033\sqrt{K}\left[\left(1 + \frac{1.739}{K}\right)^{\frac{1}{2}} - \frac{1.315}{\sqrt{K}}\right]^{-3}, \tag{5}$$

where $K = Re\sqrt{R/a}$ is the Dean number and a is the vessel curvature. Therefore, Eq. (3) is modified to

$$\mathcal{R}_v = \frac{8\mu}{\pi} \int_0^L 0.1033\sqrt{K(x)}\left[\left(1 + \frac{1.729}{K(x)}\right)^{\frac{1}{2}} - \frac{1.315}{\sqrt{K}}\right]^{-3} \frac{1}{R(x)^4}dx \tag{6}$$

Note that R, a and K generally vary as a function of x.

2.3 Expansions

The energy dissipation due to sudden expansions is taken into account by using a semi-empirical model

$$\Delta P = K_t \frac{\rho}{2A_0^2}\left(\frac{A_0}{A_s} - 1\right)^2 Q \mid Q \mid, \tag{7}$$

where A_s and A_0 are cross-sectional areas describing the expansion as described below, and $|Q|$ denotes the absolute value of flowrate in case of reverse flow. Eq. (7) with $K_t = 1$ can be derived from a control volume energy balance of inviscid flow through a sudden expansion [7]. Similar to [54], K_t is an empirical correction factor to account for losses from flow separation. We showed in a previous study [32] that $K_t = 1.52$ produced consistently accurate prediction of pressure drop compared to 3D simulations in realistic vascular (coronary) stenoses.

In this study, the local minima and maxima of $R(x)$ were computed along each vessel segment. Then A_s was computed at each local minimum and A_0 was computed from the mean value of the radius at the local maxima immediately proximal and distal to the corresponding local minimum. For vascular segments with multiple sudden expansions, these losses were added in series

$$\mathcal{R}_s = \sum_{i=1}^{n} \frac{\rho K_t}{2A_{0,i}^2}\left(\frac{A_{0,i}}{A_{s,i}} - 1\right)^2 \mid Q \mid, \tag{8}$$

where n is the number of expansions.

2.4 Bifurcations

Energy losses at vascular junctions were determined from geometric (branch angle) and hydraulic (flow split) considerations. Namely, the amount of pressure drop due to a vascular bifurcation was calculated as [34]

$$\Delta P = \frac{1}{2}\rho\frac{Q_{dat}^2}{A_{dat}^2}(1 + \lambda_j^2\psi_j^2 - 2\lambda_j\psi_j\cos(\phi_j)), \tag{9}$$

where Q_{dat} and A_{dat} are the flow rate and cross-sectional area of the datum supplier vessel, respectively. $\lambda_j = Q_j/Q_{dat}$ defines the volumetric flow split, $\psi_j = A_{dat}/A_j$ defines the area split and $\phi_j = 3(\pi - \theta_j)/4$ is defined from the angle θ_j between a datum supplier and child branch (see Figure 1 panel 2). Hence the nonlinear resistance

$$\mathscr{R}_b = \frac{1}{2Q_j}\rho\frac{Q_{dat}^2}{A_{dat}^2}(1 + \lambda_j^2\psi_j^2 - 2\lambda_j\psi_j\cos(\phi_j)) \tag{10}$$

is added in series to the resistances due to viscous and sudden expansion effects in the child branch.

2.5 Unsteadiness

Flow unsteadiness affects the momentum balance, Eq. (2), in two main ways. First, it explicitly leads to a change in fluid inertia as captured in the first term. Second, it implicitly changes the cross-sectional profile of the flow, which in turn changes the shear rate and viscous dissipation captured in the second term. To account for the later, we modify the viscous resistance according to Womersley number.

The Womersley number, $\alpha = R\sqrt{\rho\omega/\mu}$, quantifies the relative importance between pulsatile inertial effects and viscous effects. The heart rate is generally the dominant frequency and used to define ω. For image-based vascular models, ω, ρ and μ vary minimally and thus variations of α are due to variations in R. As Womersley number increases the velocity profile changes from parabolic to flat, increasing viscous losses.

Based on the well-known Womersley's solution for pulsatile flow in a straight, rigid vessel [55], wall shear stress can be computed and then used to compute the (viscous) resistance due to Womersley flow. This can be used to define a function $\zeta(\alpha)$ describing the viscous resistance ratio between Womersley and Poiseuille flow. Hence, the viscous resistance introduced in Eq. (3) is modified to

$$\mathscr{R}_v = \frac{8\mu}{\pi}\int_0^L \zeta(\alpha(x))\frac{1}{R(x)^4}dx, \tag{11}$$

where ζ is a function of x because R and hence α is a function of x. In this study we use the maximum between the curvature loss ratio γ and pulsatile loss ratio ζ in each artery to modify the Poiseuille resistance (cf. Eq. (12) below).

2.6   Implementation

Based on the above considerations, we define

$$
\mathscr{R} = \frac{8\mu}{\pi} \int_0^L \max\{\gamma, \zeta\} \frac{1}{R^4} dx + \sum_{i=1}^{n} \frac{\rho K_t}{2A_{0,i}^2} \left(\frac{A_{0,i}}{A_{s,i}} - 1\right)^2 |Q| + \frac{1}{2Q}\rho \frac{Q_{dat}^2}{A_{dat}^2}(1 \\
+ \lambda_j^2 \psi_j^2 - 2\lambda_j \psi_j \cos(\phi_j))
\tag{12}
$$

and Eq. (2) along with conservation of mass is used to solve for flow rate through each vascular segment and pressure at each vascular junction of complete (image-based) vascular model.

We have developed an in-house Python framework to automate the DLP modeling procedure. The only required inputs are the segmented geometry (i.e., surface mesh derived from medical image segmentation) and desired boundary conditions. We have developed automated procedures to generate vessel lengths, bifurcation angles, and the variation of cross-sectional area and curvature along each vascular segment. We have implemented a variety of boundary conditions typical to current state-of-the-art image-based modeling, including the ability to couple LNP models at the inlet or outlets. Once the geometry is processed and boundary conditions prescribed, the end result is a system of nonlinear AEs and ODEs that describe the basic conservation principles. An implicit Euler scheme was used to handle time-stepping. This results in a set of nonlinear algebraic equations to be solved each time-step, which is handled by iterative linearization. The solution of this system includes flow rate at all vascular segments and pressure values at all vascular junctions and boundaries. Spatially resolved representation of pressure can be derived (as shown in the Results) by linear interpolation between consecutive junctions, except in scenarios where sudden expansion occurs, in which case piecewise linear interpolation between junction(s) and expansion(s) is more appropriate. The overall DLP modeling workflow is shown in Figure 1 for a representative patient-specific coronary model.

3   Results

Here we apply the proposed DLP framework to a variety of image-based vascular models and compare the results to those derived from CFD simulation. Image-based CFD modeling was performed using SimVascular [50]. This entailed segmenting a vascular geometry from corresponding image data (also used for the DLP model), creating a volumetric mesh, employing and tuning boundary conditions representative of downstream and upstream physiology, finite element simulation of the 3D time-dependent Navier-Stokes equations, and post-processing to compute the flow rate and pressure at locations for comparison with the DLP model. All CFD simulations were run assuming rigid vessel walls. This is a common assumption in image-based hemodynamics modeling applications where information such as changes to flow distribution, perfusion, or pressure drop are primary targets. The CFD simulations used linear tetrahedral elements with boundary layer meshing for all simulations. Solutions were computed over time until the pressure fields at the inlets and outlets did not change more than 1.0-2.0% compared to the solutions at the same time point in the previous cardiac cycle. Fluid properties ($\rho = 1.06$ g/cm^3, $\mu = 0.04$ dyn/(cm^3 s))

were assumed common among all models. Appendix A describes details regarding the specification of boundary conditions unique to each group of models. The majority of these models are available at www.vascularmodel.com.

To ensure a consistent comparison between the DLP model and CFD simulation, the same inlet and outlet boundary conditions are used. However it should be noted that the DLP model is in no way tuned to the 3D CFD results; it is automated and independent of the CFD simulation. To quantify the comparison, we calculated the relative errors between the mean values of the temporal flow rate and pressure from the DLP and CFD models at the inlets and outlets of each model. These errors are plotted as box-and-whisker plots in the subsections below for each group of models. For perspective, we also compare against results from a DLP model for which a Poiseuille resistance is assumed. This model can be viewed as a "baseline" model for which the corrections to the dissipation term proposed herein are neglected.

Errors were quantified at the outlets to evaluate the ability of the DLP model to serve as a surrogate for the entire 3D domain in applications such as UQ, design optimization, parameter tuning, etc., and because these downstream locations are generally where errors are expected to become compounded. However, to better convey spatial and temporal differences between the DLP results and CFD results, we include additional comparisons of the spatial variation of the pressure field between DLP and CFD models, as well as temporal variations in the flow and pressure waveforms at the outlets. To keep the number of plots manageable, we do this only for one model for each group of models. Generally, the model chosen was the one that presented the largest errors from the box-and-whisker plots.

3.1 Aortic models

We considered four models of the ascending aorta. This region generally has complex flow patterns due to high curvature, high Reynolds number and high Womersley number. The complexity of the flow, and difficulty of CFD simulations, is increased in cases that also contain stenosis or aneurysm. The four models we considered include one normal, two with coarctation (moderate and severe), and one aneurysmal, as shown in Figure 2(I). Figure 2(II) displays relative errors of mean flow rates and pressures between the DLP model ($\bar{Q}_{0D}, \bar{P}_{0D}$) and CFD ($\bar{Q}_{3D}, \bar{P}_{3D}$) at the inlet and all outlets, demonstrating that the DLP model provides accurate prediction of mean flow rate and pressure in all cases when compared with CFD simulations. The mean value of the errors is less than 1% for all cases and the maximum error is ~1.5%. For comparison, when the baseline Poiseuille resistance is assigned to each vascular segment, the mean values of pressure ($\bar{P}_{pois}$) are significantly inaccurate, particularly for the cases with coarctation. Figure 3 shows a time-resolved comparison of flow and pressure waveforms at the inlet and all outlets of the severe coarctation model and demonstrates the ability of the DLP model to accurately calculate temporal changes in flow rate and pressure waveforms even when there exists highly complex 3D flow and severe pressure gradient.

3.2   Aorto-femoral models

We considered four aorto-femoral models. The abdominal aorta and iliac or femoral arteries are common locations for image-based CFD. This region is prone to complex flow due to significant rerouting of blood flow proximal to the abdominal segment, and propensity for aortic aneurysm or vascular disease in the distal iliac arteries. The four models considered are shown in Figure 4(I). Model A represents a non-diseased vasculature of significant spatial extent, spanning from the heart down to the femoral arteries. Model B has moderate aneurysms in both right and left common iliac arteries. Models C and D have abdominal aortic aneurysms, with notable curvature and aneurysm complexity in Model D. Figure 4(II) plots the errors in mean flow rate and pressure between the DLP and CFD models, demonstrating that the results from the DLP model are in strong agreement with CFD simulations. The mean value of the errors is less than 2% for all cases. A maximum error of ~4% occurred at the right renal artery of Model C. The mean value of the errors in pressure are increased by a factor of over 3-fold for all models when only Poiseuille resistances are used. Figure 5 provides a comparison between the temporal flow rate and pressure waveforms calculated by the DLP model and CFD simulation for Model C, which had the highest mean and maximum errors amongst the models. The temporal waveforms from the DLP model are in strong agreement with the CFD simulations, as is the general distribution of pressure.

3.3   Coronary models

We considered four patient-specific models of the proximal aorta and major coronary arteries as shown in Figure 6(I). Flow in the coronary arteries is widely studied since coronary artery disease (CAD) is the leading cause of death worldwide. Model A had a severe CAD stenosis (~80%) in the first diagonal branch as well as a mild CAD stenosis (~50%) in the middle of the left anterior descending (LAD) artery. Model B had a mild CAD stenosis (~50%) in the mid LAD. Model C represents a "healthy" vasculature with no observable CAD. Model D had mild CAD on the right side, with ~50% diameter reduction in the right coronaries at the bifurcation of the main and first marginal arteries. The mean value of the pressure errors were 5%, 2.6%, 0.7% and 0.9% for Models A, B, C, and D, respectively, as shown in Figure 6(II). A maximum error of ~10% was observed for one of the coronary branches of Model A. This maximum error occurred in a healthy branch, and not in the complex stenotic region. As shown in the right panel in Figure 6(II), errors are substantially higher when assigning the baseline Poiseuille resistance to each vascular segment. Figure 7 provides a comparison between the temporal flow rate and pressure waveforms calculated by the DLP model and CFD simulation for Model A, which had the highest mean and maximum errors amongst the models. The temporal waveforms from the DLP model are in strong agreement with the CFD simulations, including downstream from the complex stenotic regions. There is also strong agreement the distribution of pressure as shown in the top portion of Fig. 7.

3.4   Cerebrovascular models

We considered four cerebrovascular models. Flow in the cerebrovascular arteries is widely studied due to it importance to brain health and various diseases including stroke. The

models we considered were of the vertebrobasilar system, which is interesting because it contains both converging and diverging flows, and significant vessel curvatures. The four models considered are shown in Figure 8(I). All models include the left and right vertebral arteries as inlets. Figure 8(II) plots the errors in mean flow rate and pressure between the DLP and CFD models demonstrating that DLP model incurs error values less than 1% for all cases. When Poiseuille resistance is used, the maximum errors are increased by a factor of greater than 3-fold (right panel). Figure 9 provides a comparison between the temporal flow rate and pressure waveforms calculated by the DLP model and CFD simulation for Model A, which had the highest mean errors amongst the models. The temporal waveforms from the DLP model are in strong agreement with the CFD simulations as is the overall pressure distribution.

3.5 Pulmonary models

We considered four models of the pulmonary arteries, which is a region often studied in image-based CFD in the context of pulmonary hypertension and other diseases. Because the pulmonary circulation is far more compact than the systemic circulation, pulmonary models typically contain numerous bifurcations and many outlets, which leads to significant numerical challenges for CFD analysis. The four patient-specific pulmonary models extending from the main pulmonary artery to various levels of branching in the left and right pulmonary arteries (LPA, RPA) are shown in Figure 10(I). Figure 10(II) shows that the mean value of pressure errors were <3% for all pulmonary models tested. Errors increased when the baseline Poiseuille resistance was used. For example, the maximum error increased from ~10% to ~25% in one of the arteries of Model B, where the mean value of the pressure errors increase by 3-fold when the baseline Poiseuille resistance was used. This increase in error was generally less than in other groups of models though, potentially because the models were mostly composed of relatively straight-tube segments. Figure 11 provides a comparison between the temporal flow rate and pressure waveforms calculated by the DLP model and CFD simulation for Model B, which had the highest mean and maximum errors amongst the models. The results of the DLP model are in strong agreement with the CFD simulation results at all boundaries (plots a–f), and the overall distribution of pressure is consistent between the CFD and DLP models (top panel).

3.6 Pediatric surgery models

We considered four models of surgical repairs used to treat congenital heart defects. This is an area where image-based CFD has been widely utilized to understand and develop surgical procedures to improve flow re-routing and distribution. The four models considered are shown in Figure 12(I). Models A, B and C are of patients with Fontan surgery and D is from a patient with Glenn surgery. Figure 12(II) plots the errors in mean flow rate and pressure between the DLP model and CFD simulation. Mean pressure errors were 4.7%, 3.9%, 5.8% and 1.6% for Models A, B, C, and D, respectively. The maximum error for all cases was <10% except for Model C, which had a maximum error of ~15%. As shown in Figure 12(II), this maximum error significantly increased to ~ 40% when the baseline Poiseuille resistance was used. Figure 13 provides a comparison between the temporal flow rate and pressure waveforms calculated by the DLP model and CFD simulation for Model C, which had the highest errors amongst the models, and two severe area reductions in the IVC and LPA

branches. The results of the DLP model are in strong agreement with the CFD simulation results at all boundaries, as is the overall pressure distribution between the CFD and DLP results.

4 Discussion

We have presented a framework to predict vessel-level temporal flow rate and pressure waveforms in 3D image-based vascular models. The proposed DLP framework provided consistent prediction with CFD simulations with mean errors <7% over a range of cardiovascular modeling applications. This framework is fully automated based on an input model geometry (and specification of boundary conditions), and generally requires approximately 1/1000 of the computational cost of corresponding CFD simulations. On a single CPU core, it took 334 ± 49 seconds to complete all steps of the DLP framework (steps 1-5 in Figure 1) over the range of models presented in this work (with most processing occurring in step 1 and 2). However, the framework was implemented in Python, whereas the SimVascular flowsolver is implemented in Fortran, which is more optimized for compute speed. Thus additional saving are expected if the proposed DLP is implemented in a lower level language and optimized for performance. Also, it is important to note that the nonlinearity of the Navier-Stokes equations coupled with common cardiovascular boundary conditions results in numerical challenges that, in practice, can necessitate multiple CFD simulations before meaningful results are obtained (e.g. tuning of solver settings or initial conditions). The DLP framework is generally not prone to such numerical challenges. Thus, "compute time" may be a conservative depiction of CFD time cost.

To the best of the authors' knowledge, this is the most comprehensive comparisons of a ROM to the current standard of image-based CFD modeling. We considered a diverse range of image-based vascular anatomies, geometric features, and flow dynamics. Namely, the two key non-dimensional parameters of Reynolds number and Womersley number varied from approximately 100-3000 and 1-20, respectively. Vessel sizes ranged from approximately 0.15 cm to 2 cm in diameter. These ranges in Reynolds number, Womersley number and vessel diameter span a broad spectrum of expected values encountered in most image-based computational hemodynamics modeling studies. In addition to the dynamic and geometric differences explored, the number of vascular junctions across the models varied from 4 to 96. The junctions include both converging and diverging flows, where converging flows sometimes result in a negative loss coefficient [34], and in presence of back flow, some bifurcations can have both diverging and converging flows at different time points of the cardiac cycle–factors that are handled in our implementation. Additionally, vascular expansions, as quantified by the area reduction ratio $1 - A_s/A_0$, ranged up to approximately 90%, and the mean curvature ratio $\delta = R/a$ ranged up to approximately 0.5 over models considered, which again covers a broad range of expected values.

In many application, fully-resolved CFD is essential to determine spatial variations in field variables. For example, this is generally necessary to resolve wall shear stress variations important to disease progression [17, 15, 4, 3] or detailed analysis of local flow topology or transport [41, 40, 39]. However, in many image-based CFD applications, the primary objective is to compute integrated quantities such as pressure drop across a stenosis [45, 26],

flow rerouting [20, 53, 11], etc. In such applications, 3D time-dependent PDE-based modeling may not be essential. This conclusion is not otherwise obvious, however, since one might expect that a full Navier-Stokes solve is needed to resolve the complex flow structures that determine energy dissipation. Nonetheless, the DLP model appears to reasonably predict these losses through basic relations that can be solved quickly. While some error is incurred, it is instructive to put the observed levels of error in context. Notably, all simulations carry some level of error from modeling assumptions, and uncertainty in parameters or boundary conditions [37, 10, 12]. For example, due to limits in image resolution, a geometry segmented from image data will carry inherent uncertainty. For demonstrative purposes, we considered the uncertainty in minimum lumen diameter (MLD) of the 80% stenosis in coronary Model A using a mean MLD error as reported in [14] and re-ran the CFD simulation. Figure 14 demonstrates that the deviation in pressure prediction between the DLP model and CFD model is well within the error of the CFD results due to this particular geometric uncertainty alone.

Unlike most fitting-based ROM strategies (machine learning, basis functions expansions, etc.), the proposed DLP framework provides mechanistic insight into the contributions of various sources of energy dissipation. Based on the variety of models considered, we note that the modification due to flow separation downstream of expansions, when present, has the highest contribution to accurately predict flow and pressure in the corresponding model. Viscous dissipation introduced by curvature generally has the second highest contribution in energy losses. This can be confirmed by comparing the second and third panels of error plots for coronary models, which had negligible unsteadiness effects, particularly for the healthy coronaries of Model C. Similarly, for the cerebrovascular models the results were improved most by considering curvature effects, as $\alpha \approx 2$ in these models, and there were no stenotic segments. It was generally found that Womersley effects have the next highest impact, where for example viscous resistance increases by up to ~5-fold in the aortic models. The Womersley effect can be seen for example in the aorto-femoral models where the errors approximately tripled without considering this effect. While in [13] losses due to bifurcations were found to improve hemodynamics modeling, the results herein indicated that the other sources of energy loss are more significant, except potentially in models where numerous junctions exist, such as for the pulmonary models. For representative purposes, Appendix B provides distribution of the explicit resistance values obtained from a coronary DLP model.

The major potential impact of the work presented here is two-fold. First, given the relative accuracy of the DLP approach, it could be potentially replace CFD simulation in applications where time is of the essence. This broadens the possibilities for image-based modeling in clinical scenarios. Secondly, a major impact of this approach is to applications where numerous CFD simulations would be desirable, such as for model parameter or boundary condition tuning [48], uncertainty quantification [10], sensitivity analysis [16], surgery/device design [21], data assimilation [52], machine learning training [25], etc. In such scenarios, it could be the de facto model, or used in conjunction with more expensive CFD simulations to reduce the number of full CFD model evaluations. This could be highly significant as the above types of ensemble-based engineering analyses are playing an increasing role in image-based modeling research and translational applications [31]. We

also note that although the current DLP framework does not account for vessel deformability and wave propagation phenomenon it could possibly be used in conjunction with quasi-1D PDE models that are better suited for such analysis. Namely, quasi-1D models are known to perform poorly in locations of complex flow [32] (e.g. expansions, curvature, etc.), partly because a developed velocity profile must be assumed. The DLP model presented here could alternatively be used to modify loss factors in the quasi-1D equations such that more realistic flow conditions could be better considered by these long-standing models.

Acknowledgements

Appendix

A   Model boundary conditions

This section describes the specification of boundary conditions for all models. Further description on the boundary conditions, as well as imaging and available model data, are posted at www.vascularmodel.com. All of the CAD models are available at this site, except the four coronary models, which are uploaded as part of the electronic supplementary material.

A.1   Aortic models

Phase-contrast (PC) MRI was used to measure volumetric flow in the ascending aorta and the respective waveforms for each patient (see inset panels in Figure 2(I)) was mapped to the inlet of the CFD models using a time varying parabolic flow profile as the inflow boundary condition. Three-element "RCR" Windkessel models were coupled at all outlets. Information regarding how to choose the RCR parameters for each outlet are detailed in [28]. Regional mesh refinement was in the aortic coarctation models to resolve the complex flow features in the stenotic region.

A.2   Aorto-femoral models

For Model A, an aortic flow waveform was adapted from [35] to have a mean cardiac output of 4.6 L/min (female). For Model B the supraceliac aorta blood flow waveform was derived from PC-MRI. For Models C and D individualized inflow boundary conditions were determined based on the Baker equation [5], relating body surface area to cardiac output, and assuming that ~70% of the cardiac output is distributed to the supraceliac aorta [36]. The resulting mean flows were used to generate inflow waveforms by scaling a gender-matched representative supraceliac aortic flow waveform. RCR models were applied at each outlet. The RCR parameters for each outlet were determined based on flow distributions to the outlets obtained from clinical PC-MRI measurements for Model B, or from literature data [33] for Models A, C and D.

A.3 Coronary models

In all cases, aortic flow was prescribed at the inlet, an RCR of the systemic circulation was coupled at the aortic outlet, and coronary-specific LPNs (see Figure 6(I)) that consider the time-dependent intramyocardial pressure were coupled at each coronary outlet (separate LPN for each outlet). The effect of intramyocardial pressure is modeled by scaling the typical left and right ventricular pressures to recover realistic coronary flow waveforms. The LPN parameters of the systemic and coronary outlets were tuned to match target pressure and flow splits to the aorta and systemic and coronary outlets. A detailed description of the tuning procedure is given in [38]. Mesh refinement was used in all cases with stenotic lesions.

A.4 Cerebrovascular models

For all models, a characteristic vertebral blood flow waveform from the literature [18] was scaled to match time-averaged PC-MRI measurements in the vertebral arteries and mapped to a time-varying parabolic profile at the model inlet. Resistance boundary conditions were used at the outlets. A total resistance was calculated and distributed amongst the outlets by assuming all outlets act in parallel with resistance values inversely proportional to the outlet area. More details on boundary conditions are given in [11].

A.5 Pulmonary models

Pulmonary blood flow waveforms from PC-MRI were applied to the inlet of each model. The inflow waveforms were manipulated to have zero back flow to avoid numerical instability in the CFD simulations. Resistance values were assigned at the outlets based on the estimated mean pressure values for each patient, cross sectional area of the outlets, and left to right pulmonary flow split ratio obtained from PC-MRI data. Detailed description of resistance tuning for the pulmonary modeling is given in [44].

A.6 Congenital heart disease models

PC-MRI data was used to prescribe an inflow waveform to the inlets of computational domains. Inflow waveforms prescribed at the inferior and superior vena cava (IVC, SVC), internal jugular vein (IJV) and broncheocephilic vein (BrS) are shown in Figure 12(I) for all models. RCR models were coupled to each outlet, which parameters tuned to match target pressure values and assuming the LPA/RPA flow split ratio to be 45/55 for all patients. All numerical values for boundary condition parameters are available at www.vascularmodel.com.

B   Representative example of DLP modeling results

A representative example of the computed resistance values from DLP modeling are presented for better understanding the relative contribution of various sources of energy dissipation. Table 1 shows resistance values at systole determined from the patient-specific coronary simulation shown in Figure 7 .

References

[1]. Acosta S, Puelz C, Riviere B, Penny D, and Rusin C. Numerical method of characteristics for one-dimensional blood flow. J. Comput. Phys, 294:96–109, 2015. [PubMed: 25931614]

[2]. Arzani A and Shadden S. Characterization of the transport topology in patient-specific abdominal aortic aneurysm models. Phys. Fluids, 24:081901, 2012.

[3]. Arzani A and Shadden SC. Wall shear stress fixed points in cardiovascular fluid mechanics. Journal of Biomechanics, 73:145–152, 2018. [PubMed: 29625775]

[4]. Arzani A, Suh GY, Dalman RL, and Shadden SC. A longitudinal comparison of hemodynamics and intraluminal thrombus deposition in abdominal aortic aneurysms. American Journal of Physiology-Heart and Circulatory Physiology, 307(12):H1786–H1795, 2014. [PubMed: 25326533]

[5]. Baker S, Verweij J, Rowinsky E, Donehower R, Schellens J, Grochow L, and Sparreboom A. Role of body surface area in dosing of investigational anticancer agents in adults, 1991-2001. J. Natl. Cancer Inst, 94(24):1883–1888, 2002. [PubMed: 12488482]

[6]. Barnard A, Hunt W, Timlake W, and Varley E. A theory of fluid flow in compliant tubes. Biophys. J, 6(6):717–724, 1966. [PubMed: 5972373]

[7]. Batchelor G. An introduction to fluid dynamics. Cambridge University Press, New York, 2000.

[8]. Bianchi M, Marom G, Ghosh R, Rotman O, Parikh P, Gruberg L, and Bluestein D. Patient-specific simulation of transcatheter aortic valve replacement: impact of deployment options on paravalvular leakage. Biomech. Model. Mechanobiol, 18(2):435–451, 2018. [PubMed: 30460623]

[9]. Blanco P, Watanabe S, Passos M, Lemos P, and Feijoo R. An anatomically detailed arterial network model for one-dimensional computational hemodynamics. IEEE Trans. Biomed. Eng, 62(2):736–753, 2015. [PubMed: 25347874]

[10]. Boccadifuoco A, Mariotti A, Celi S, Martini N, and Salvetti M. Impact of uncertainties in outflow boundary conditions on the predictions of hemodynamic simulations of ascending thoracic aortic aneurysms. Comput. Fluids, 165:96–115, 2018.

[11]. Bockman M, Kansagra A, Shadden S, Eric C, and Marsden A. Fluid mechanics of mixing in the vertebrobasilar system: Comparison of simulation and mri. Cardiovasc. Eng. Tech, 3(4):450–461, 2012.

[12]. Bruning J, Hellmeier F, Yevtushenko P, Khne T, and Goubergrits L. Uncertainty quantification for non-invasive assessment of pressure drop across a coarctation of the aorta using cfd. Cardiovasc. Eng. Technol, 9(4):582–596, 2018. [PubMed: 30284186]

[13]. Chnafa C, Valen-Sendstad K, Brina O, Pereira V, and Steinman D. Improved reduced-order modelling of cerebrovascular flow distribution by accounting for arterial bifurcation pressure drops. J. Biomech, 51:83–88, 2017. [PubMed: 27986327]

[14]. Choi G, Uzu K, Toba T, Mori S, Takaya T, Shinke T, Roy A, Nguyen T, Khem S, Taylor C, and Otake H. Accuracy of lumen boundary extracted from coronary CTA for calcified and noncalcified plaques assessed using OCT data. J. Am. Coll. Cardiol, 66, 2015.

[15]. Deplano V, Knapp Y, Bertrand E, and Gaillard E. Flow behaviour in an asymmetric compliant experimental model for abdominal aortic aneurysm. J. Biomech, 40:2406–2413, 2007. [PubMed: 17258220]

[16]. Eck V, Donders W, Sturdy J, Feinberg J, Delhaas T, Hellevik L, and Huberts W. Uncertainty quantification, sensitivity analysis, cardiovascular modeling, monte carlo, polynomial chaos, fractional flow reserve, arterial compliance. Int. J. Numer. Method Biomed. Eng, 32(8):e02755, 2016.

[17]. Finol E and Amon C. Blood flow in abdominal aortic aneurysms: pulsatile flow hemodynamics. J. Biomech. Engng, 123(5):474–484, 2001. [PubMed: 11601733]

[18]. Ford M, Alperin N, Lee S, Holdsworth D, and Steinman D. Characterization of volumetric flow rate waveforms in the normal internal carotid and vertebral arteries. Physiol. Meas, 26(4):477–488, 2005. [PubMed: 15886442]

[19]. Ghigo A, Fullana J, and Lagre P. A 2d nonlinear multiring model for blood flow in large elastic arteries. J. Comput. Phys, 350:136–165, 2017.

[20]. Grinberg L, Cheever E, Anor T, Madsen J, and Karniadakis G. Modeling blood flow circulation in intracranial arterial networks: A comparative 3d/1d simulation study. Ann. Biomed. Eng, 39(1):297–309, 2010. [PubMed: 20661645]

[21]. Gundert T, Marsden A, Yang W, and LaDisa J. Optimization of cardiovascular stent design using computational fluid dynamics. J. Biomech. Eng, 134(1):011002, 2012. [PubMed: 22482657]

[22]. Hughes T and Lubliner J. On the one-dimensional theory of blood flow in the larger vessels. Math. Biosci, 18(1):161–170, 1973.

[23]. Inzoli F, Migliavacca F, and Mantero S. Pulsatile flow in an aorto-coronary bypass 3-d model. Biofluid Mechanics Proceedings of the 3rd International Symposium, 1994.

[24]. Ito H. Laminar flow in curved pipes. J. Appl. Math. Mech, 49(11):653–663, 1969.

[25]. Itu L, Rapaka S, Passerini T, Georgescu B, Schwemmer C, Schoebinger M, Flohr T, Sharma P, and Comaniciu D. A machine-learning approach for computation of fractional flow reserve from coronary computed tomography. J. Appl. Physiol, 121(1):42–52, 2016. [PubMed: 27079692]

[26]. Itu L, Sharma P, Ralovich K, Mihalef V, Ionasec R, Everett A, Ringel R, Kamen A, and Comaniciu D. Non-invasive hemodynamic assessment of aortic coarctation: validation with in vivo measurements. Ann. Biomed. Eng, 41(4):669–681, 2013. [PubMed: 23232558]

[27]. Joly F, Soulez G, Garcia D, Lessard S, and Kauffmann C. Flow stagnation volume and abdominal aortic aneurysm growth: Insights from patient-specific computational flow dynamics of lagrangian-coherent structures. Comput. Biol. Med, 92:98–109, 2018. [PubMed: 29169074]

[28]. LaDisa J, Figueroa A, Vignon-Clementel I, Kim h., Xiao N, Ellwein L, Chan F, Feinstein J, and Taylor C Computational simulations for aortic coarctation: Representative results from a sampling of patients. J. Biomech. Eng, 133(9):091008, 2011. [PubMed: 22010743]

[29]. LaDisa J, Guler I, Olson L, Hettrick D, Kersten J, Warltier D, and Pagel P. Three-dimensional computational fluid dynamics modeling of alterations in coronary wall shear stress produced by stent implantation. Ann. Biomed. Eng, 31(8):972–980, 2003. [PubMed: 12918912]

[30]. Mantero S, Pietrabissa R, and Fumero R. The coronary bed and its role in the cardiovascular system: a review and an introductory single-branch model. J. Biomed. Eng, 14:109–116, 1992. [PubMed: 1564919]

[31]. Marsden A. Optimization in cardiovascular modeling. Annu. Rev. Fluid Mech, 46:519–546, 2014.

[32]. Mirramezani M, Diamond S, Litt H, and Shadden S. Reduced order models for transstenotic pressure drop in the coronary arteries. J. Biomech. Eng, 141(3):031005, 2018.

[33]. Moore J and Ku D. Pulsatile velocity measurements in a model of the human abdominal aorta under resting conditions. J. Biomech. Eng, 116:337–346, 1994. [PubMed: 7799637]

[34]. Mynard J and Valen-Sendstad K. A unified method for estimating pressure losses at vascular junctions. Int. J. Numer. Meth. Biomed. Engng, 31(7), 2015.

[35]. Olufsen M, Peskin C, Kim W, Pedersen E, Nadim A, and Larsen J. Numerical simulation and experimental validation of blood flow in arteries with structured-tree outflow conditions. Ann. Biomed. Eng, 28(11):1281–1299, 2000. [PubMed: 11212947]

[36]. Reymond P, Merenda F, Perren F, Rufenacht D, and Stergiopulos N. Validation of a one-dimensional model of the systemic arterial tree. Am. J. Physiol. Heart. Circ. Physiol, 297(1):208–222, 2009.

[37]. Sankaran S, Kim H, Choi G, and Taylor C. Uncertainty quantification in coronary blood flow simulations: Impact of geometry, boundary conditions and blood viscosity. J. Biomech, 49(12):2540–2547, 2016. [PubMed: 26803339]

[38]. Sankaran S, Moghadam M, Kahn A, Tseng E, Guccione J, and Marsden A. Patient-specific multi-scale modeling of blood flow for coronary artery bypass graft surgery. Ann. Biomed. Eng, 40(10):2228–2242, 2012. [PubMed: 22539149]

[39]. Shadden SC and Arzani A. Lagrangian postprocessing of computational hemodynamics. Annals of Biomedical Engineering, 43(1):41–58, 2015. [PubMed: 25059889]

[40]. Shadden SC and Hendabadi S. Potential fluid mechanic pathways of platelet activation. Biomechanics and Modeling in Mechanobiology, 12(3):467–474, 2013. [PubMed: 22782543]

[41]. Shadden SC and Taylor CA. Characterization of coherent structures in the cardiovascular system. Annals of Biomedical Engineering, 36:1152–1162, 2008. [PubMed: 18437573]

[42]. Sherwin S, Franke V, Peiro J, and Parker K. One-dimensional modelling of a vascular network in space-time variables. J. Eng. Math, 47(3):217–250, 2003.

[43]. Song X, Throckmorton A, Wood H, Allaire P, and Olsen D. Transient and quasi-steady computational fluid dynamics study of a left ventricular assist device. Asaio. J, 50(5):410–417, 2004. [PubMed: 15497378]

[44]. Tang B, Fonte T, Chan F, Tsao P, Feinstein J, and Taylor C. Three dimensional hemodynamics in the human pulmonary arteries under resting and exercise conditions. Ann. Biomed. Eng, 39(1):347–358, 2011. [PubMed: 20640512]

[45]. Taylor C, Fonte T, and Min J. Computational fluid dynamics applied to cardiac computed tomography for noninvasive quantification of fractional flow reserve: scientific basis. J. Am. Coll. Cardiol, 66(22):2233–2241, 2013.

[46]. Taylor C and Steinman D. Image-based modeling of blood flow and vessel wall dynamics: Applications, methods and future directions. Ann. Biomed. Eng, 38:1188–1203, 2010. [PubMed: 20087775]

[47]. Toy S, Melbin J, and Noordergraaf A. Reduced models of arterial systems. IEEE Trans. Biomed. Eng, 32:174–176, 1985. [PubMed: 3997173]

[48]. Tran J, Schiavazzi D, Ramachandra A, Kahn A, and Marsden A. Automated tuning for parameter identification and uncertainty quantification in multi-scale coronary simulations. Comput. Fluids, 142:128–138, 2017. [PubMed: 28163340]

[49]. Tse K, Chiu P, Lee H, and Ho P. Investigation of hemodynamics in the development of dissecting aneurysm within patient-specific dissecting aneurismal aortas using computational fluid dynamics (cfd) simulations. J. Biomech, 44(5):827–836, 2011. [PubMed: 21256491]

[50]. Updegrove A, Wilson N, Merkow J, Lan H, Marsden A, and Shadden S. Simvascular: an open source pipeline for cardiovascular simulation. Ann. Biomed. Eng, 45(3):525–541, 2017. [PubMed: 27933407]

[51]. Wan Ab Naim W, Ganesan P, Sun Z, Lei J, Jansen S, Hashim S, Ho T, and Lim E. Flow pattern analysis in type b aortic dissection patients after stent-grafting repair: Comparison between complete and incomplete false lumen thrombosis. Int. J. Numer. Method Biomed. Eng, 34:2961, 2018.

[52]. Wang J, Xiao H, and Shadden S. Data-augmented modeling of intracranial pressure. Ann. Biomed. Eng, 47(3):714–730, 2019. [PubMed: 30607645]

[53]. Yang W, Feinstein JA, Shadden SC, Vignon-Clementel IE, and Marsden AL. Optimization of a Y-graft design for improved hepatic flow distribution in the Fontan circulation. Journal of Biomechanical Engineering, 135(1):011002, 2013. [PubMed: 23363213]

[54]. Young D and Tsa F. Flow characteristics in models of arterial stenoses-i. steady flow. J. Biomech 6(4):403–410, 1973.

[55]. Zamir M. The Physics of Pulsatile Flow. Springer-Verlag, New York, 2000.
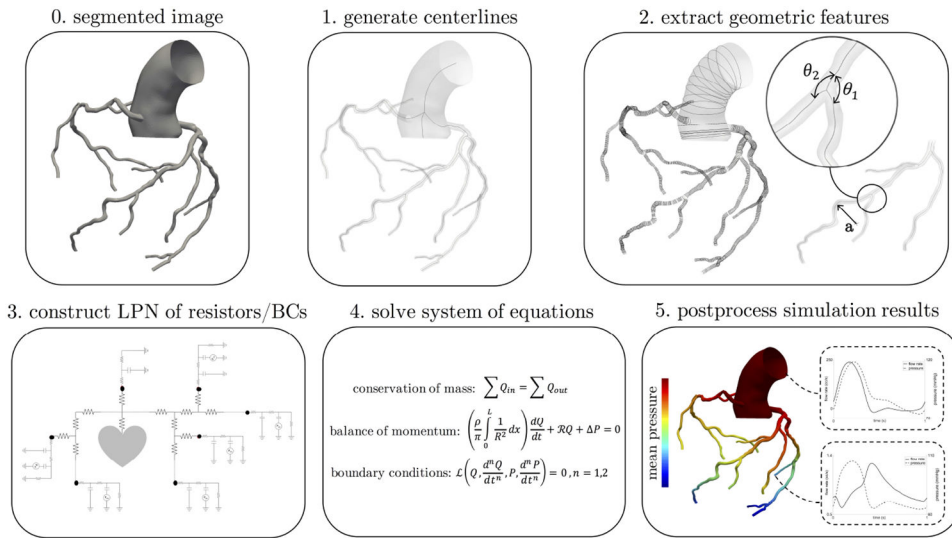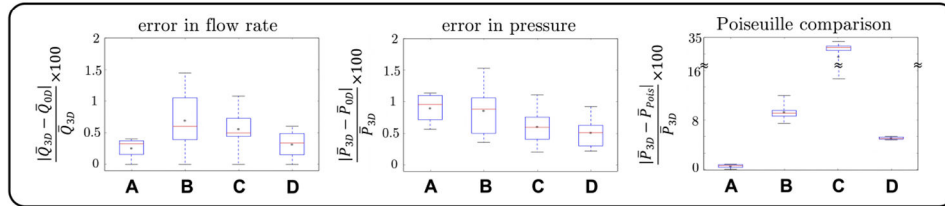
Figure 1:

The modeling steps of the automated framework to compute blood flow and pressure in a representative patient-specific coronary model using the proposed DLP method.
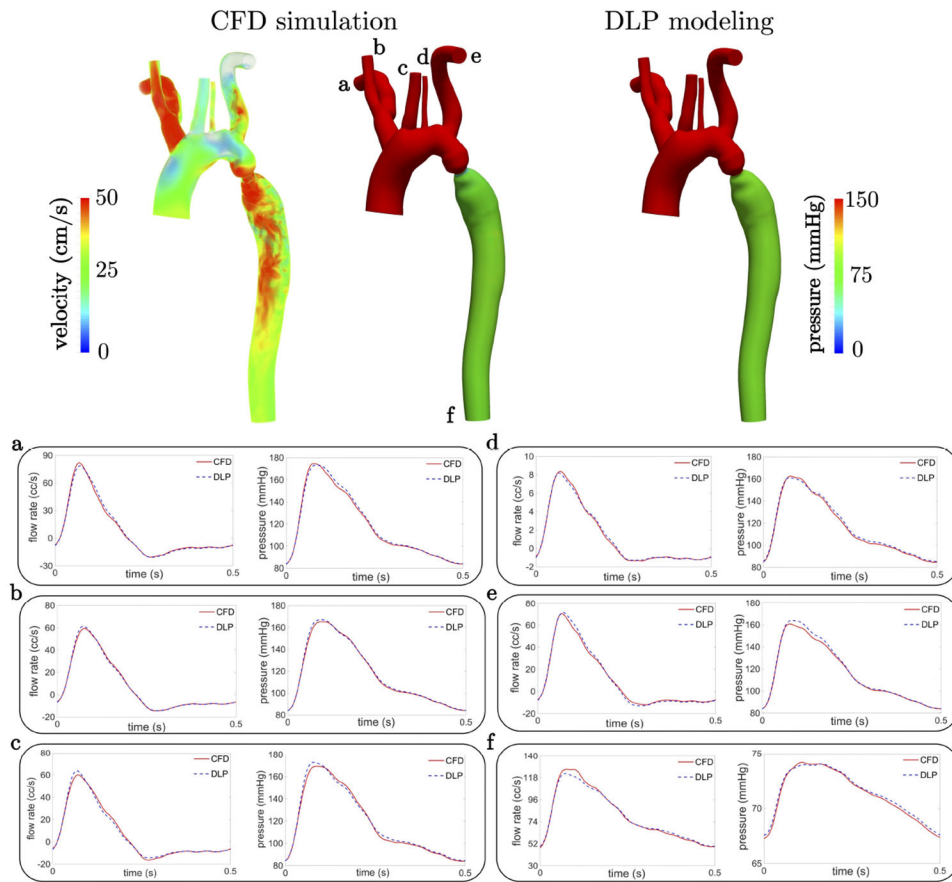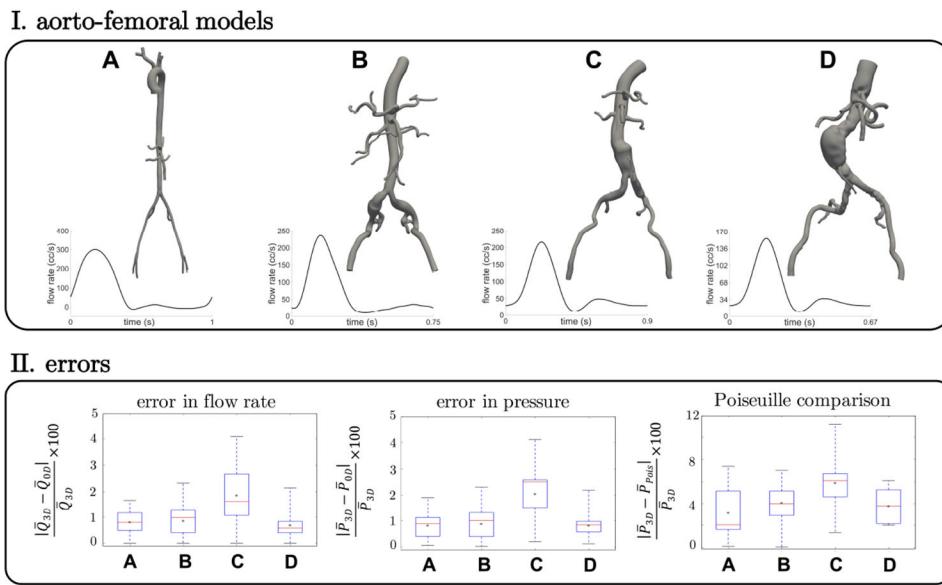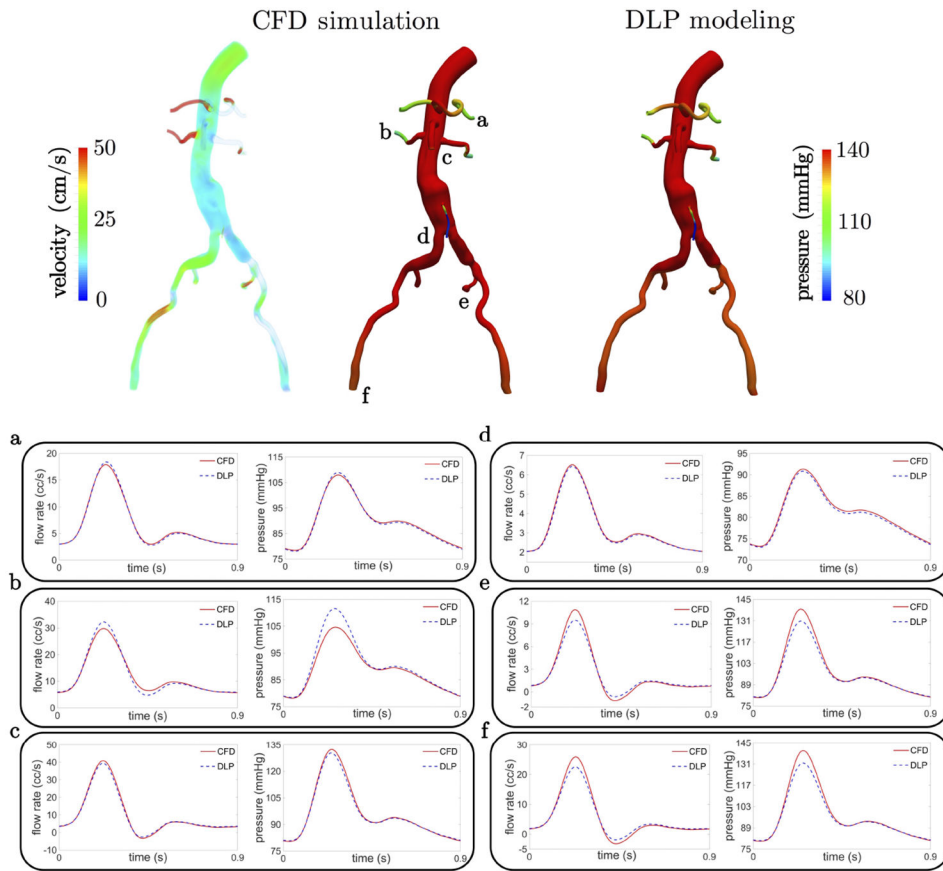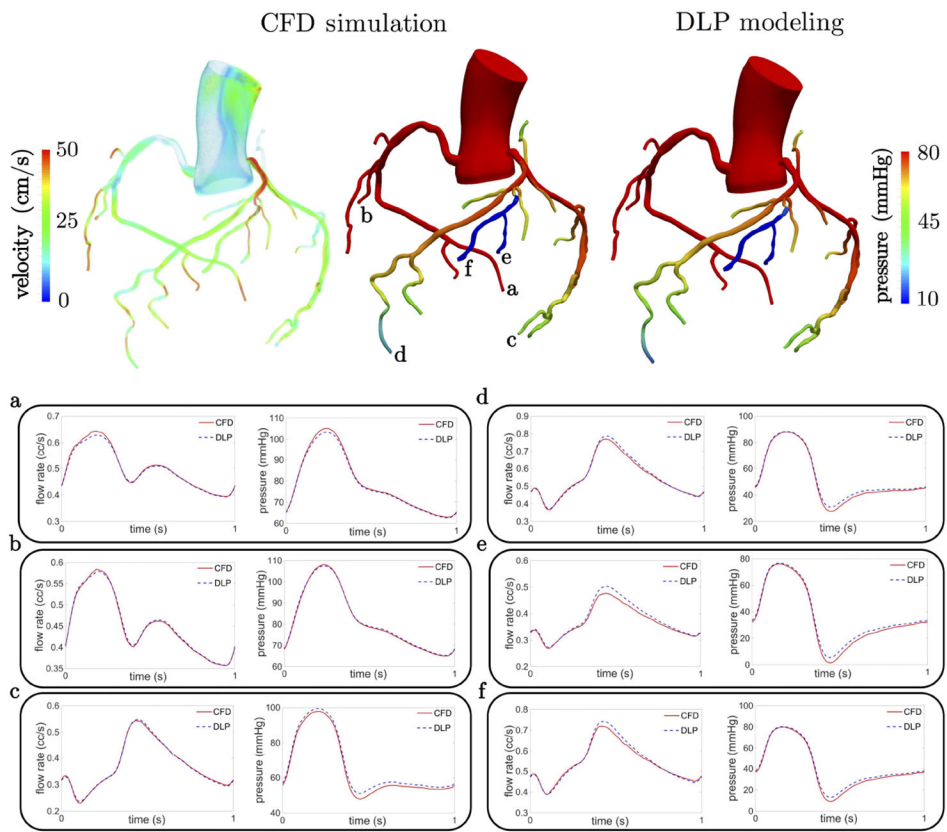
I. aorta models
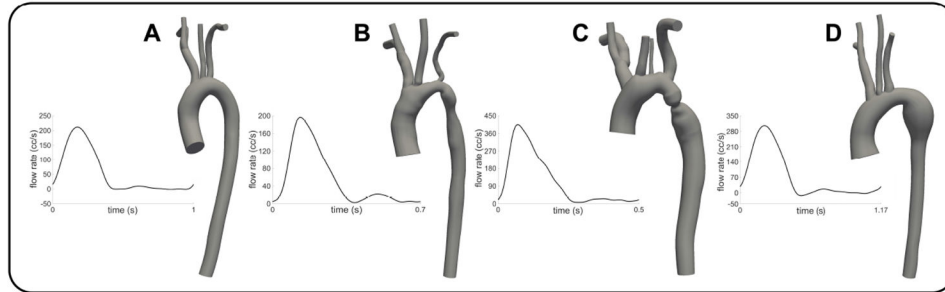
II. errors

Figure 2:
I. Aorta models and their inflow waveforms. **II.** Errors in mean flow rate (left) and pressure (middle) between DLP model ($\bar{Q}_{0D}, \bar{P}_{0D}$) and CFD simulation ($\bar{Q}_{3D}, \bar{P}_{3D}$) across inlets and outlets. Right panel are errors of baseline Poiseuille resistance DLP model ($\bar{P}_{pois}$).

Figure 3:
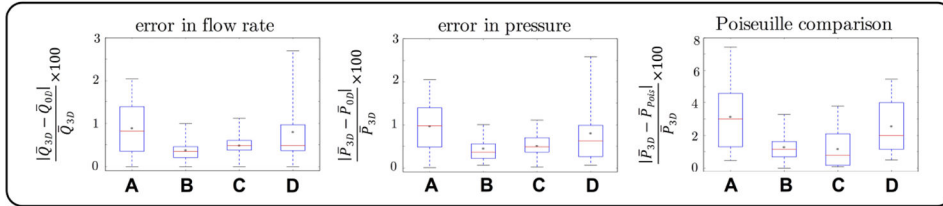Pressure and velocity fields in aortic Model C during systole, and comparisons of flow rate and pressure waveforms between DLP model ("DLP") and CFD simulation ("CFD") at representative outlets.
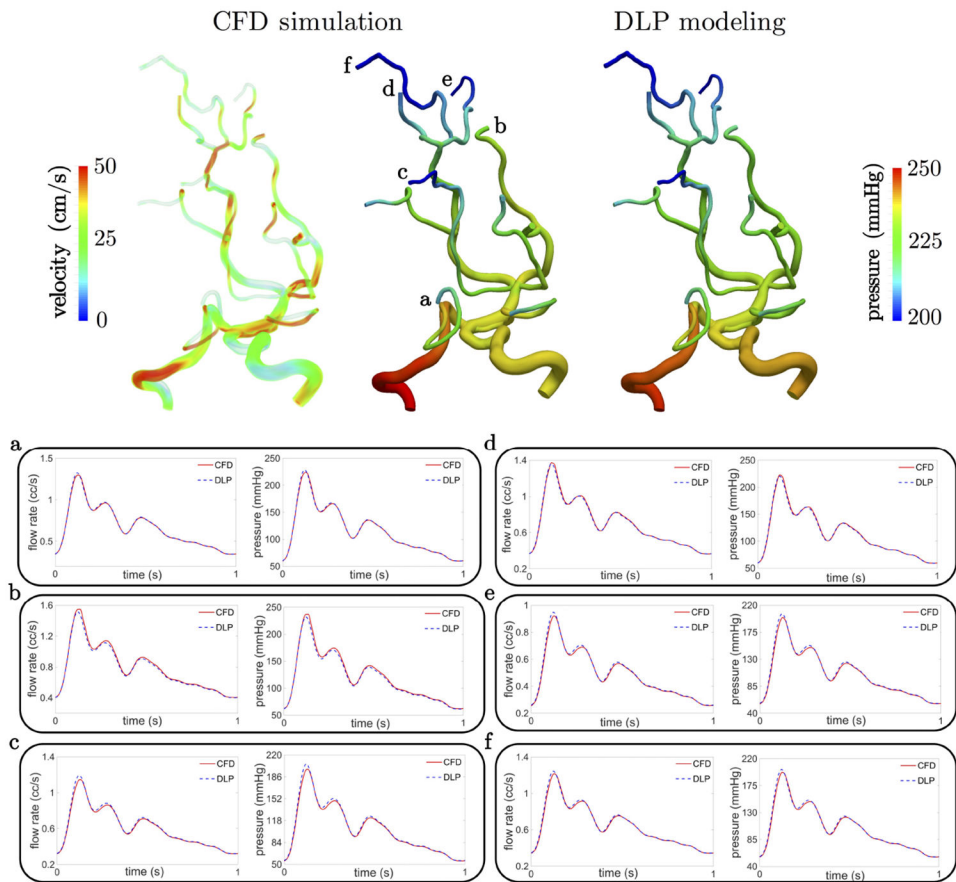
I. aorto-femoral models

II. errors

Figure 4:

I. Aorto-femoral models and their inflow waveforms. **II.** Errors in mean flow rate (left) and pressure (middle) between the DLP model ($\bar{Q}_{0D}$, $\bar{P}_{0D}$) and CFD simulation ($\bar{Q}_{3D}$, $\bar{P}_{3D}$) across inlets and outlets of each model. Right panel are errors of baseline Poiseuille resistance DLP model ($\bar{P}_{pois}$).

Figure 5:
Pressure and velocity fields of aorto-femoral Model C at systole, and comparisons of flow rate and pressure waveforms between DLP model ("DLP") and CFD simulation ("CFD") at representative outlets.
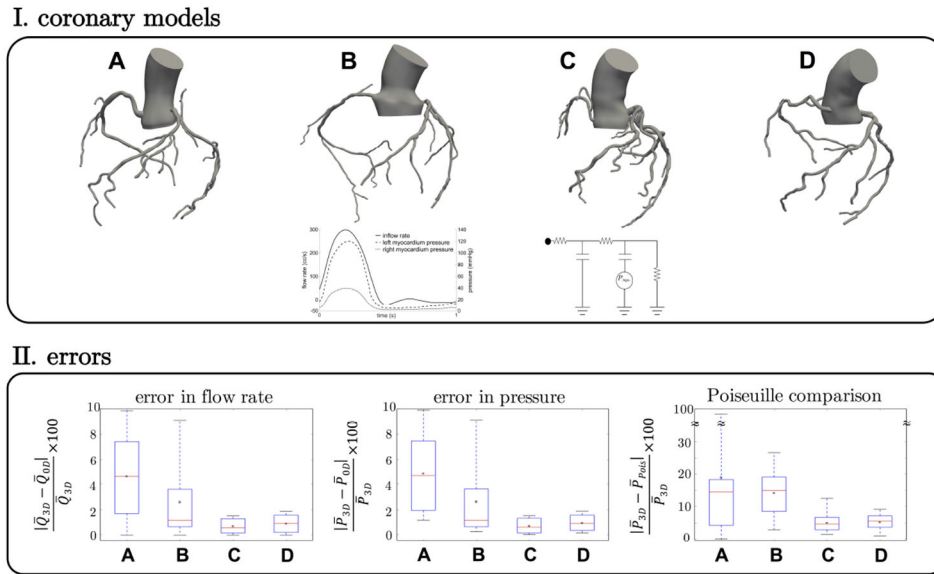
Figure 6:
I. Coronary models and prescribed inflow and pressure waveforms for coronary LPNs. **II.** Errors in mean flow rate (left) and pressure (middle) between DLP model ($\bar{Q}_{0D}$, $\bar{P}_{0D}$) and CFD simulation ($\bar{Q}_{3D}$, $\bar{P}_{3D}$) over inlets and outlets of each model. Right panel are errors of baseline Poiseuille resistance DLP ($\bar{P}_{pois}$).
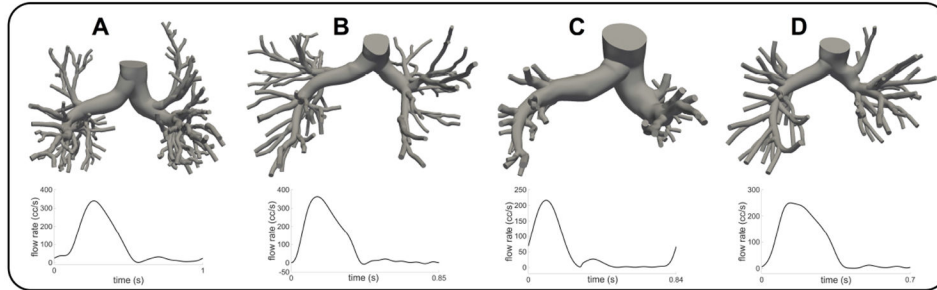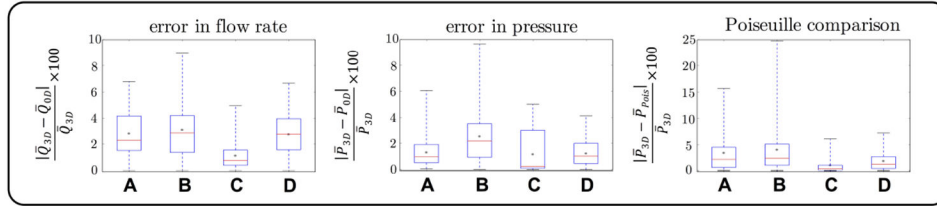
Figure 7:
Pressure and velocity fields of coronary Model A at early diastole, and comparisons of flow rate and pressure waveforms of DLP model ("DLP") and CFD simulation ("CFD") at representative outlets.
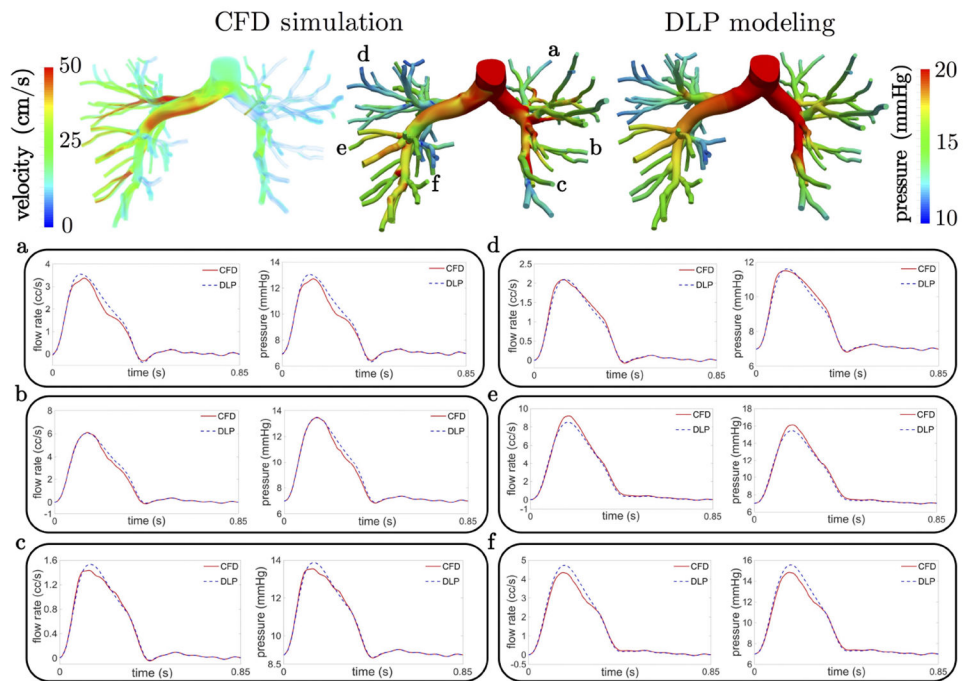
I. cerebrovascular models
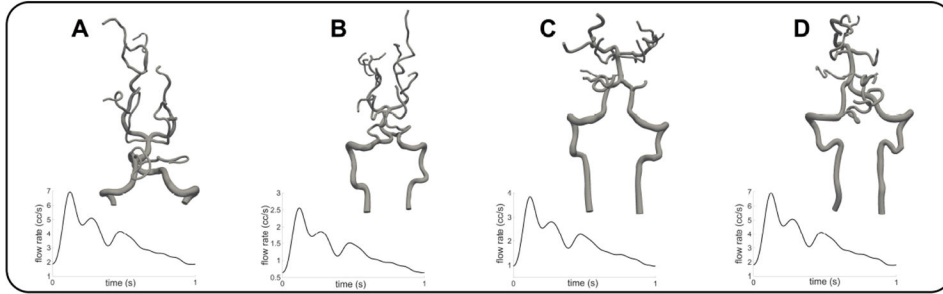
II. errors

Figure 8:
I. Cerebrovascular models and their inflow waveforms. **II.** Errors of mean flow rate (left) and pressure (middle) between DLP model ($\bar{Q}_{0D}, \bar{P}_{0D}$) and CFD simulation ($\bar{Q}_{3D}, \bar{P}_{3D}$) at inlets and outlets of each model. Right panel are errors of baseline Poiseuille resistance DLP ($\bar{P}_{pois}$).

Figure 9:
Pressure and velocity fields in the cerebrovascular Model A at systole, and comparisons of flow rate and pressure waveforms from DLP model ("DLP") and CFD simulation ("CFD") at representative outlets.
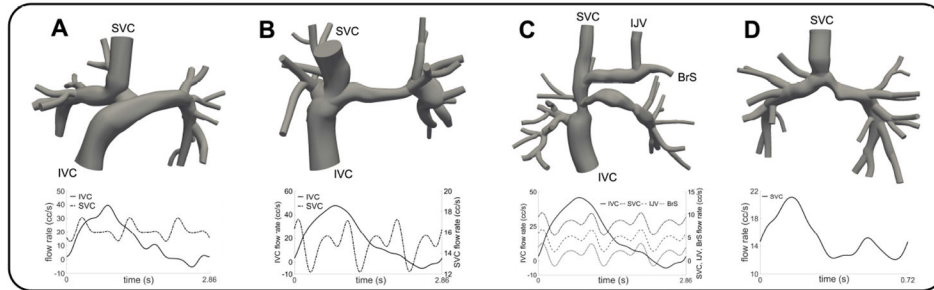
I. pulmonary models

II. errors

Figure 10:
I. Pulmonary models and their inflow waveforms. **II.** Errors of mean flow rate (left) and pressure (middle) between DLP model ($\bar{Q}_{0D}$, $\bar{P}_{0D}$) and CFD simulation ($\bar{Q}_{3D}$, $\bar{P}_{3D}$) at inlets and outlets of each model. Right panel are errors of baseline Poiseuille resistance DLP ($\bar{P}_{pois}$).
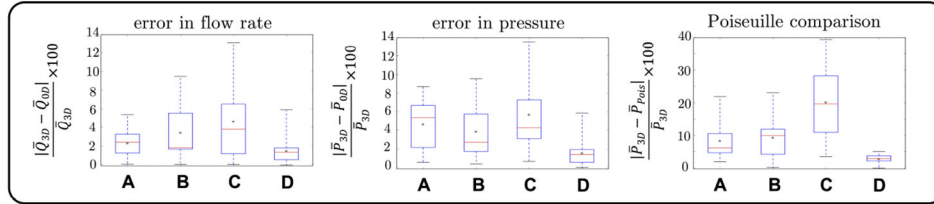
Figure 11:
Pressure and velocity fields of the pulmonary Model B at systole, and comparisons of flow rate and pressure waveforms from DLP model ("DLP") and CFD simulation ("CFD") at representative outlets.
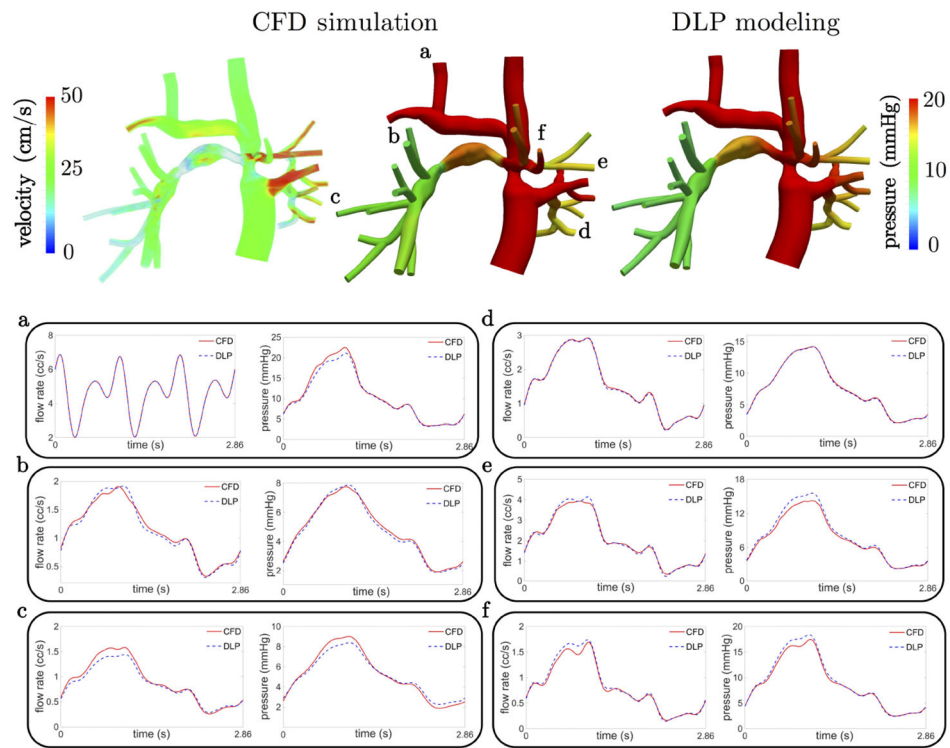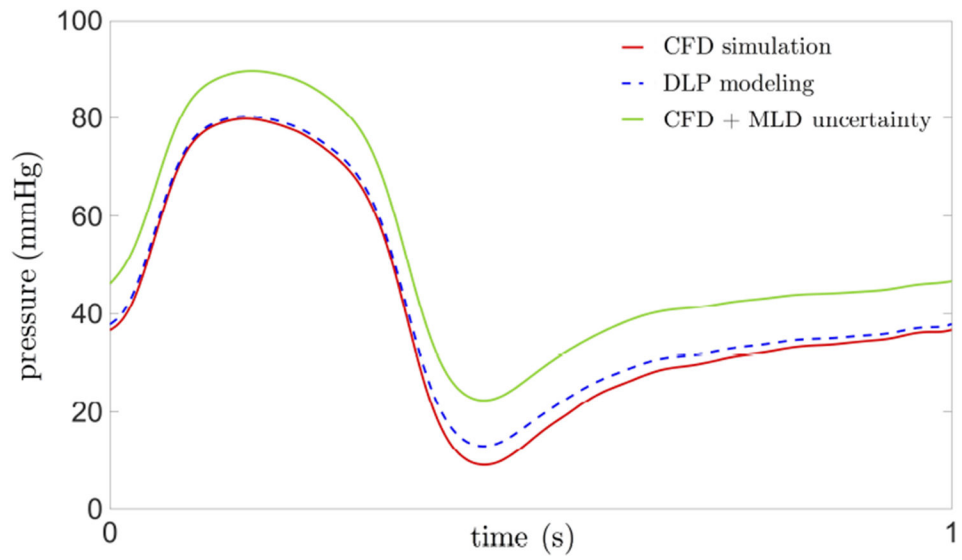
Figure 12:
I. Pediatric surgery models and their time-varying inflow waveforms. **II.** Errors of mean flow rate (left) and pressure (middle) between DLP model ($\bar{Q}_{0D}$, $\bar{P}_{0D}$) and CFD simulation ($\bar{Q}_{3D}$, $\bar{P}_{3D}$) at inlets and outlets of each model. Right panel are errors of baseline Poiseuille resistance DLP ($\bar{P}_{pois}$).
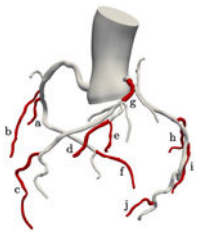
Figure 13:
Systolic pressure and velocity fields of the Fontan surgery Model C, and comparisons of flow rate and pressure waveforms from DLP model ("DLP") and CFD simulation ("CFD") at representative outlets.

Figure 14:
Pressure waveform from the DLP model, original CFD, and CFD considering minimum lumen diameter (MLD) uncertainty of the ~80% stenosis of coronary Model A, cf. Figure. 7(f).

Table 1:

Resistance values in cgs units ($g/s \cdot cm^4$) at systole from DLP modeling for patient-specific coronary simulation shown in Figure 7. R_v: viscous resistance, R_c: curvature resistance, R_u: unsteadiness resistance, R_s: expansion resistance, R_b: bifurcation resistance, R_t: total resistance, $R_{Pois.} = \frac{8\mu L}{\pi \bar{r}^4}$ ($\bar{r}$: mean radius).

coronary model	label	R_v	max$\{R_c, R_u\}$	R_s	R_b	R_t	$R_{Pois.}$
	a	6343	4322	3372	1159	15195	5332
	b	18442	5850	3163	82	27537	16358
	c	29840	7835	8951	1076	47702	21557
	d	4978	1851	823	2436	10089	4705
	e	18277	2549	3591	13423	37840	14539
	f	9586	2318	1033	391	13329	7227
	g	1312	1494	268	197	3271	1273
	h	17185	8751	4641	334	30911	13717
	i	20037	7881	5273	1267	34458	12006
	j	11741	3266	1712	4772	21493	9830